Detection of Germanium Nanocrystals as Tracer Materials in Polypropylene via Raman Spectroscopy

Monique Greiner * , Michael Pohlitz , Philipp Kitschke , Aylin Last , Christian K. Müller , Jonathan G. C. Veinot , Michael Heinrich

Posted Date: 8 May 2026

doi: 10.20944/preprints202605.0524.v1

Keywords: Germanium Nanocrystals, Polypropylene, Composites, Raman spectroscopy, Tracer technology, Digital material passport

 doi:10.20944/preprints202605.0524.v1

Article

Detection of Germanium Nanocrystals as Tracer Materials in Polypropylene via Raman Spectroscopy

Monique Greiner [1,*], Michael Pohlitz [2], Philipp Kitschke [2], Aylin Last [2], Christian K. Müller [2], Jonathan G. C. Veinot [3] and Michael Heinrich [1]

[1] Institute for Production Technology, Faculty of Automotive and Mechanical Engineering, University of Applied Sciences Zwickau, Germany; Monique.Greiner@whz.de (M. G.), Michael.Heinrich@whz.de (M. H.)

[2] Leupold Institute of Applied Sciences, Faculty of Physical Engineering/Computer Sciences, University of Applied Sciences Zwickau, Germany Michael.Pohlitz@whz.de (M. P.), Philipp.Kitschke@whz.de (P. K.), Aylin.Last@whz.de (A. L.), Christian.Mueller.1@whz.de (C. K. M.)

[3] Department of Chemistry, University of Alberta, Chemistry, Edmonton, Canada; jveinot@ualberta.ca (J. V.)

* Correspondence: Monique.Greiner@whz.de (M. G.)

Highlights

- utilization of Germanium Nanocrystals (GeNCs) as tracer materials for polymers.
- synthesis and functionalization with dodecyl ligands of hydride-terminated GeNCs.
- integration of GeNCs into polypropylene in different concentrations.
- Spatially resolved Raman mapping of GeNCs in polypropylene.

Abstract

Increasing regulatory demands for high-quality plastic recycling create a strong need for novel tracer systems that enable reliable polymer identification and sorting. This feasibility study evaluates germanium nanocrystals (GeNCs) as Raman-detectable tracer materials in polypropylene (PP). The synthesis of GeNC/PP composite materials possessing various GeNC contents via a solvent-based intercalation process followed by compounding and injection molding is reported. Hydride-terminated GeNCs were synthesized and subsequently functionalized with dodecyl ligands to ensure chemical stability, compatibility with the polymer matrix, and processability under conventional melt-processing conditions. The dodecyl-functionalized GeNCs were successfully stabilized and homogeneously integrated into the PP matrix. Raman spectroscopy demonstrates the clear detection of GeNCs within the composites through a characteristic Ge–Ge optical phonon mode at 296 cm^{-1}, which is well separated from the intrinsic Raman bands of polypropylene. The Raman signal intensity increases systematically with increasing GeNC concentration. Raman mapping reveals an overall homogeneous distribution of the nanocrystals within the polymer, while a slight tendency toward agglomeration is observed at higher loadings. These results demonstrate that GeNCs are well suited as optically detectable tracers for polypropylene and can be reliably identified using Raman spectroscopy, highlighting their potential for tracer-based sorting concepts in advanced recycling and digital material passport applications.

Keywords: germanium nanocrystals; polypropylene; composites; raman spectroscopy; tracer technology; digital material passport

1. Introduction

Recent European Union regulations, including the Packaging and Packaging Waste Regulation (PPWR) and the Circular Economy Action Plan, mandate substantial increases in recycling rates and the use of recycled content in new products [1, 2]. The volume of plastic waste is projected to double

 doi:10.20944/preprints202605.0524.v1

by 2050 [3], underscoring the urgent need to enhance recycling rates. Currently, just under 50 % of post-consumer plastics waste in Europe undergoes thermal utilization rather than mechanical or chemical recycling [4]. A significant factor contributing to these low recycling rates are the inherent limitations of conventional sorting processes, which predominantly rely on near-infrared (NIR) spectroscopy. Black plastics, which are frequently used in technical applications, cannot be identified to any great extent using NIR [5]. High-quality recyclates necessitate well-sorted waste streams that account not only for polymer type but also for the presence of additives, fillers, and reinforcement materials such as fibers [6]. The accurate identification of these components typically requires the integration of multiple analytical technologies. To overcome the limitations of conventional sorting facilities alternative methods such as Fourier transform infrared spectroscopy (FTIR) , Raman-spectroscopy, laser-induced breakdown spectroscopy(LIBS), X-ray fluorescence spectroscopy (XRFS), hyperspectral Imaging, terahertz imaging, and machine learning to improve mentioned detection systems were investigated [7].

Another promising approach for improved sorting is tracer-based sorting (TBS), whereby the detection system does not identify the plastic itself by its characteristics but rather a tracer material with specific optical features. The idea to use photoluminescent tracers for plastics identification and sorting first occurred in a patent in 1991 [8]. Since then, suitable marking materials and analysis or sorting methods as well as various options for integrating or applying the tracer materials in or on the plastic products have been investigated. These tracer materials include, among others, rare earth oxides (lanthanides), Carbon Quantum Dots and supraparticles with a magnetic fingerprint, as well as intrinsically luminescent polymer-based materials. However, tracer material-specific disadvantages such as toxicity and poor photostability were identified. [9–12]

The TBS concept allows creating an optical fingerprint that acts as a material passport, encoding information about polymer types, regardless of color, as well as details regarding additives, fillers and other constituents. Utilizing such advances may help to reduce greenhouse gas emissions by enabling higher mechanical and chemical recycling rates as alternatives to thermal recovery. Moreover, cross-contamination with hazardous substances, such as flame retardants, throughout the recycling process can be omitted. As a result, highly refined waste streams yielding superior-quality recyclates suitable for high-value applications, including electronics housings and automotive components, are available and thereby reducing the dependence on virgin materials.

While the TBS concept demonstrates considerable potential, the practical implementation requires tracer materials that combine excellent optical properties with non-toxicity, photostability, and processability. Among the emerging alternatives, semiconductor nanocrystals (NCs) represent an attractive option in this regard. These materials have received significant interest due to their tunable properties making them attractive for sophisticated modern applications such as bio-imaging, sensors, lasers, light emitting diodes, memory elements, and for energy conversions [13–16]. Their potential applications are wide-ranging, including use as materials for nanostructured light sources, sensors, field-effect transistors, solar cells, security technologies, imaging processes and drug delivery in biological systems [13–24]. However, the most widely studied NCs are based upon toxic elements such as Pb, Cd or Hg [25], which limits the practical utility based upon these systems insofar as their acceptance as materials for everyday applications. In contrast, Group 14 semiconductors (i.e., Si and Ge) are abundant, possess the same size-tunable properties of other NCs, and reports indicate that nanomaterials based upon these elements are non-toxic [13, 14, 21, 26]. Intensive research into the targeted surface functionalization of Group 14 nanocrystals, particularly silicon nanocrystals (SiNCs), has been conducted over the past few decades [27–40]. Recently, studies based on this research have been published, presenting the use of functionalized SiNCs in modern applications such as product security (anti-counterfeiting) and photodynamic cancer therapy [41, 42]. Moreover, composite materials consisting of SiNCs and polymeric materials can be produced without any segregation effects occurring. This allows the unique optoelectronic features of the SiNCs to be combined with the properties of the polymer matrix [43–45]. In contrast, studies focusing on the practical use of GeNCs are rarely reported, with most research centering on their application in the

 doi:10.20944/preprints202605.0524.v1

modern semiconductor industry, for instance in solar cells [46, 47] and quantum computing [48, 49]. To the best of our knowledge, the incorporation of GeNCs into an organic polymer matrix has only been reported once, by Uyar and coworker. In this study, an electrospinning technique was used to give a composite material based on GeNCs and polyvinyl alcohol nanofibers (GeNC/PVA) that combine the optoelectrical properties of the GeNCs with the features of the PVA matrix [50]. The latter as well as the studies reporting on the manufacturing of SiNCs/polymer composite materials using tailor-made surface-functionalized SiNCs motivated us to investigate whether this general concept could be applied using surface-functionalized GeNCs for marking and identifying bulk plastics for their recyclable use.

Here, we report on the synthesis of composite materials via a solvent-based intercalation process using dodecyl-functionalized GeNCs and commercially available polypropylene (PP) granules. Using a masterbatch approach, PP composites with different GeNC contents are compounded and further processed into test specimens using injection molding technology. Based on the obtained GeNC/PP composites, we demonstrate that dodecyl-functionalized GeNCs can be used to mark plastics and facilitate their identification during the recycling process using Raman spectroscopy as a reliable analysis method. Raman spectroscopy was found to be a suitable analytical method because spectroscopic fingerprints of GeNCs can be easily distinguished from the characteristic vibrations of polymers. These spectroscopic fingerprints can be adjusted with respect to wavenumber by varying the size of the NCs, allowing the use of defined NCs for specific polymers. In a further step, the adjustable spectral fingerprints allow to obtain spectral material passports that enable the identification of the type of polymer as well as other compounds such as additives or fillers. However, the present study focuses on the integration and detection of GeNCs in polypropylene via Raman spectroscopy as a step towards the development of NC-based material passports. To the best of our knowledge, this work represents the first successful demonstration of this concept in GeNC/bulk polymer composites, opening new opportunities for advanced material identification and traceability.

2. Materials and Methods

2.1. Materials

Germanium dioxide powder (GeO_2, 99.9 %) was purchased from ChemPur Feinchemikalien und Forschungsbedarf GmbH (Karlsruhe, Germany). Hypophosphorous acid (50 $wt\%$ in H_2O) and 1-dodecene (97 %) were purchased from Thermo Fisher GmbH (Darmstadt, Germany). Sodium hydroxide pellets, reagent grade methanol, toluene, mesitylene ethanol, *n*-hexane, hydrofluoric acid (HF, 49 % aqueous solution), hydrochloric acid (37 %), ammonium hydroxide solution (28 - 30 %) and Polytetrafluorethylen (PTFE) syringe filters ($d_{pore} = 0.45\,\mu m$) were purchased from VWR International GmbH (Darmstadt, Germany). A virgin polypropylene homopolymer (Sabic® PP 571P) was purchased from PiO Kunststoffe GmbH (Freiburg im Breisgau, Germany). All reactions were performed under argon using standard Schlenk techniques or in a glovebox. Solvents were purified and dried by applying standard techniques. The reactions were carried out with solvents that were freshly distilled from appropriate drying reagents immediately prior usage. Unless otherwise indicated reagents were used as received.

Hydride-terminated germanium nanocrystals (H-GeNCs) were obtained starting from GeO_2 powder according to a synthesis protocol being reported by Veinot and coworkers previously [51]. Please note that the synthesis of the Ge@GeO_2 hybrid material and the consecutively formed H-GeNCs were performed in the absence of silicon grease avoiding any source of silicon atom contamination for the final products. The H-GeNCs were always freshly liberated from Ge@GeO_2 hybrid materials (about $100\,mg$) by HF etching and freed from residual solvents under vacuum ($p \sim 10^{-2}\,mbar$) for at least one hour after work-up procedure and before usage. Starting from $m \sim 100\,mg$ of Ge@GeO_2 hybrid material gave on average $m \sim 31\,mg$ of H-GeNCs as brown powder.

 doi:10.20944/preprints202605.0524.v1

2.2. Material Characterization and Instrumentation

Fourier transform infrared spectroscopy was performed using a Nicolet Magna 750 IR spectrophotometer (Thermo Fisher Scientific, Darmstadt, Germany). Samples were drop-cast from suspensions containing the material in question using either *n*-hexane or toluene as liquid phase. X-ray powder diffraction (PXRD) was carried out using an INEL XRG 3000 X-ray diffractometer (Thermo Fisher Scientific, Darmstadt, Germany) equipped with a Cu-Kα radiation source ($\lambda = 1.54$ Å) and CPS-120 detector. The crystallite size was estimated using the *Scherrer* equation: $\tau = \frac{K\lambda}{\beta cos\theta}$ here τ is the volume weighted crystallite size, *K* is the *Scherrer* constant here taken as 0.94, λ is the X-ray wavelength, θ is the Bragg angle in ° and β is the full width of the diffraction line at half of the maximum intensity (FWHM, background subtracted). Bright-field transmission electron microscopy (TEM) and energy dispersive X-ray (EDX) analyses were performed using a JEOL-2010 (LaB_6 filament) electron microscope (JEOL, Freising, Germany) with an accelerating voltage of $200\ kV$. TEM samples of GeNCs were prepared by drop-coating of 1 – 3 drops of a dilute dispersion containing the material of interest using either *n*-hexane or toluene as liquid phase onto a holey carbon coated copper grid (300 mesh, Electron Microscopy Science). Bright-field TEM images were processed using ImageJ software (version 1.51s). Particle size distributions were determined by measuring at least 500 nanocrystals. Raman spectroscopy for the analysis of the functionalized GeNCs was carried out using a Renishaw in*Via* Raman microscope (Renishaw, Gloucestershire, United Kingdom) equipped with a $514\ nm$ diode laser and a power of $3.98\ mW$ on the sample. Samples were prepared by mounting the dispersions on either gold-coated glass, copper foil or silicon wafers. Raman measurements of the GeNC/PP composites were carried out using an Oxford RISE confocal Raman microscope (Oxford Instruments, Abingdon, United Kingdom). Excitation was provided by a $532\ nm$ laser operated at $0.6\ mW$ to avoid photothermal effects in the polypropylene matrix. Single-point spectra were collected with an integration time of $0.7\ s$ and 100 accumulations. Raman mapping was performed over a $30\ x\ 30\ \mu m^2$ region using $80\ x\ 80$ pixels, with an integration time of $0.6\ s$ per pixel. Raw spectra were pre-processed by cosmic-ray removal and smoothed using the instrument's built-in filter. X-ray photoelectron spectra were acquired in energy spectrum mode at $210\ W$, using a Kratos Axis Ultra X-ray photoelectron spectrometer. X-ray source was Al (Mono) Kα line with an energy of $1486.6\ eV$. The probing area was about $2\ mm^2$. Samples were prepared as films by drop-casting suspensions of the material in question in either *n*-hexane or toluene onto copper foil substrates. Binding energies were calibrated using the C 1s peak as a reference (284.8 eV). CasaXPS Version 2.3.18PR1.0 software was used for X-ray photoelectron spectroscopy (XPS) data analyses. Peak fitting was performed after background subtraction (Shirley type). The high-resolution Ge 3d region of the XP spectra has been collected for all samples investigated and were fitted to Ge $3d_{3/2}$ / Ge $3d_{5/2}$ partner lines with spin-orbit splitting fixed at $0.58\ eV$, and the Ge $3d_{3/2}$ / Ge $3d_{5/2}$ intensity ratio was set to 0.67.

Graphical images of analytical data were created using the Origin® Pro program package [52] and chemical structures were depicted using the ChemDraw [53] program package.

2.3. Synthesis of dodecane-terminated GeNCs

H-GeNCs ($\sim 31\ mg$) were dispersed in 1-dodecene ($\sim 10\ mL$) under argon and three freeze-pump-thaw cycles [a cycle is defined as follows: freezing the dispersion using liquid nitrogen until the liquid became a solid; then applying vacuum ($p \sim 10^{-2}\ mbar$) for at least $15\ min$ followed by heating the mixture to ambient temperature] were performed. The cloudy, oxygen-free reaction mixture was then heated to $190\ °C$ overnight with stirring. The dodecane-terminated GeNCs were isolated and purified using a solvent/antisolvent precipitation procedure. The crude reaction mixture was transferred to polypropylene centrifuge tubes and about $45\ mL$ of an ethanol/methanol ($v/v \sim 1/1$) mixture acting as antisolvent was added. The resulting cloudy brown suspension was centrifuged at $6000\ rpm$ for $10\ min$ to yield a brown precipitate and a transparent supernatant. The supernatant was discarded by decantation. The brown precipitate was redispersed by ultrasonic

 doi:10.20944/preprints202605.0524.v1

treatment in a minimum volume of toluene ($\sim 2\,mL$). Subsequently, methanol ($\sim 50\,mL$) was added to yield a cloudy suspension that was centrifuged at $6000\,rpm$ for $10\,min$ to yield a brown precipitate and a clear supernatant. The supernatant was discarded by decantation. The latter suspension/centrifugation procedure was repeated one more time. The resulting precipitate was then redispersed by ultrasonic treatment either in *n*-hexane (for further analysis) or in mesitylene (for further use in synthesis). Yield (on average): $m = 61\,mg$.

Further treatment of the dodecyl-functionalized GeNCs dispersed in *n*-hexane prior analyses: The dispersion was allowed to age for at least $15\,h$ resulting in sedimentation of non-stable particles. The cloudy supernatant was isolated using a syringe and then filtered using a PTFE syringe filter ($d_{pore} = 0.45\,\mu m$) to give a stable dispersion of surface-functionalized GeNCs in *n*-hexane being used for analyses. Please note that a glass syringe was used instead of any other plastic syringes to avoid contamination of the final product by chemicals such as softeners.

2.4. Synthesis of the GeNC/PP Composite (Masterbatch Preparation)

A homogeneous suspension of dodecyl-functionalized GeNCs ($\sim 54\,mg$) in mesitylene ($\sim 1\,mL$) was added to a solution of polypropylene ($\sim 470\,mg$) in mesitylene ($\sim 7.5\,mL$) at $130\,°C$, with stirring of the reaction mixture throughout. Removal of all volatiles under reduced pressure ($3\,mbar$) at $75\,°C$ gave GeNC/PP composite material as a grey powder. For Raman measurements $\sim 82\,mg$ were extracted which leads to a yield of: $m = 442\,mg$.

2.5. Manufacturing of GeNC/PP Test Specimens

Prior to processing, the polymer materials were dried at $100\,°C$ for $24\,h$. Four batches with varying GeNC concentrations were prepared by diluting a masterbatch containing $10.31\,wt\%$ GeNCs with virgin polypropylene (PP). The total weight of each batch was maintained at approximately $6150\,mg$ which corresponds to the processing capacity of the compounder utilized.

Table 1 summarizes the composition and target tracer concentrations for each batch. Thermal stability of the NCs is given as polymer processing is carried out at temperatures $\leq 190\,°C$, which is the functionalization temperature of the GeNCs.

Table 1. Composition and tracer concentrations of the prepared batches.

Batch	Target concentration ($wt\%$)	Tracer material GeNCs (mg)	Masterbatch (mg)	Polypropylene (mg)	Total weight (mg)
B01	-	-	-	6154.0	6154.0
C01	0.06	3.5	34.5	6117.5	6151.5
C02	0.23	14.0	136.1	6017.7	6153.7
C03	0.46	28.1	272.3	5873.4	6145.4

Compounding was performed using a Thermo Scientific HAAKE MiniLab 3 twin-screw extruder (Thermo Electron, Karlsruhe, Germany) equipped with co-rotating screws. Each batch was processed at a barrel temperature of $190\,°C$ and a screw speed of $100\,rpm$. The material was recirculated over an integrated backflow channel and a bypass valve within the compounder for $150\,s$ to ensure homogeneous dispersion of the GeNCs throughout the polymer matrix.

The compounded polymer melt was subsequently extruded directly into the heated cylinder of a Thermo Scientific HAAKE MiniJet Pro injection molding machine (Thermo Electron, Karlsruhe, Germany). Disc-shaped specimens with a diameter of $20\,mm$ and a thickness of $1.5\,mm$ were fabricated via injection molding. The cylinder temperature was maintained at $190\,°C$, while the mold temperature was set to $50\,°C$. An injection pressure of $100\,bar$ was applied for $5\,s$, followed by a holding pressure of $150\,bar$. The Injection molded specimens containing 0 wt% (B01), 0.06 wt%

 doi:10.20944/preprints202605.0524.v1

(C01), 0.23 wt% (C02) and 0.46 wt% (C03) GeNCs in **Figure 1** appear opaquer with increasing GeNC content. On a macroscopic scale the distribution of the GeNCs seems homogeneous.

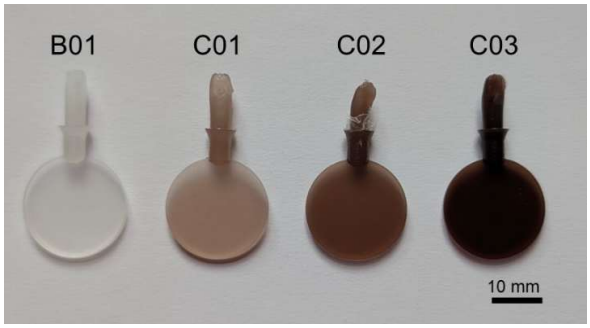

Figure 1. Injection molded specimens containing *0 wt%* (B01), *0.06 wt%* (C01), *0.23 wt%* (C02) and *0.46 wt%* (C03) GeNCs.

3. Results and Discussion

3.1. Synthesis and Characterization of GeNCs

Dodecyl-functionalized GeNCs were synthesized starting from freshly prepared hydride-terminated GeNCs (H-GeNCs) using a thermal hydrogermylation reaction according to synthesis protocols being reported by Veinot and coworkers [40]. A brief outline of a combined protocol is given as follows. Reduction of GeO_2 gave "$Ge(OH)_2$", which was annealed at *400 °C* for an hour to form a $Ge@GeO_2$ hybrid material containing GeNCs. Liberation of the GeNCs was performed by an etching process applying HF resulting in H-GeNCs (**Scheme 1a**). Freshly prepared H-GeNCs were always used for further functionalization reactions. Solvent-freed H-GeNCs were suspended in 1-dedecene and heated to *190 °C* overnight to carry out the thermal hydrogermylation reaction for the alkyl-functionalization of the GeNCs. The dodecyl-functionalized GeNCs were isolated by a solvent/antisolvent precipitation procedure. They were then used, without any further chemical modification, to prepare the GeNCs/PP composite via a solvent-assisted intercalation process (**Scheme 1b**).

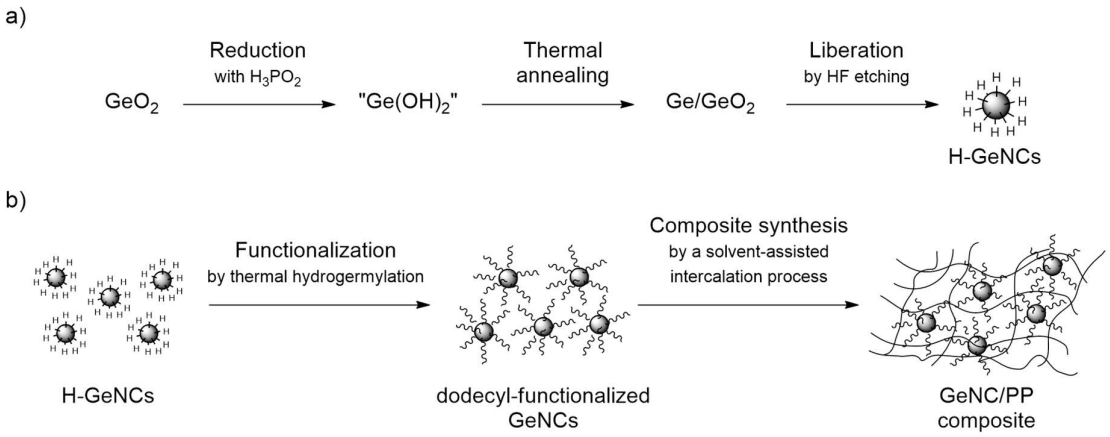

Scheme 1. Synthesis of a) H-GeNCs starting from GeO2 according to a procedure reported by Veinot and coworkers [40] and b) preparation of the GeNCs/PP composite using dodecyl-functionalized GeNCs, which were obtained by a thermal hydrogermylation reaction of H-GeNCs.

The dodecyl-functionalized GeNCs were characterized using FTIR spectroscopy, TEM, XRD, XPS and Raman spectroscopy (**Figure 2** and Figures S 1 – 3). All analytical data confirm the formation

 doi:10.20944/preprints202605.0524.v1

of alkyl-functionalized GeNCs and are in agreement with the values reported in the literature [40, 47, 50, 54]. FTIR spectroscopy analysis indicates that the hydride surface functions (H-Ge) of the H-GeNCs (intermediates) have been fully converted into dodecyl groups by the hydrogermylation reaction. The absorption band centered at $\bar{\nu} = 820\ cm^{-1}$ is assigned to residual germanium oxide species resulting from incomplete etching during the liberation process (**Figure 2a**). The latter is supported by XRD data. Reflections of low intensity that are attributed to GeO_2 were detected for the dodecyl-functionalized GeNCs (Figure S 1). A representative bright-field transmission electron microscopy (TEM) image of the dodecyl-terminated GeNCs is shown in **Figure 2b**. The particles appear pseudospherical with average diameters (determined by counting at least 500 particles) slightly larger than $7\ nm$ (**Figure 2c**) agreeing with XRD data (Figure S 1).

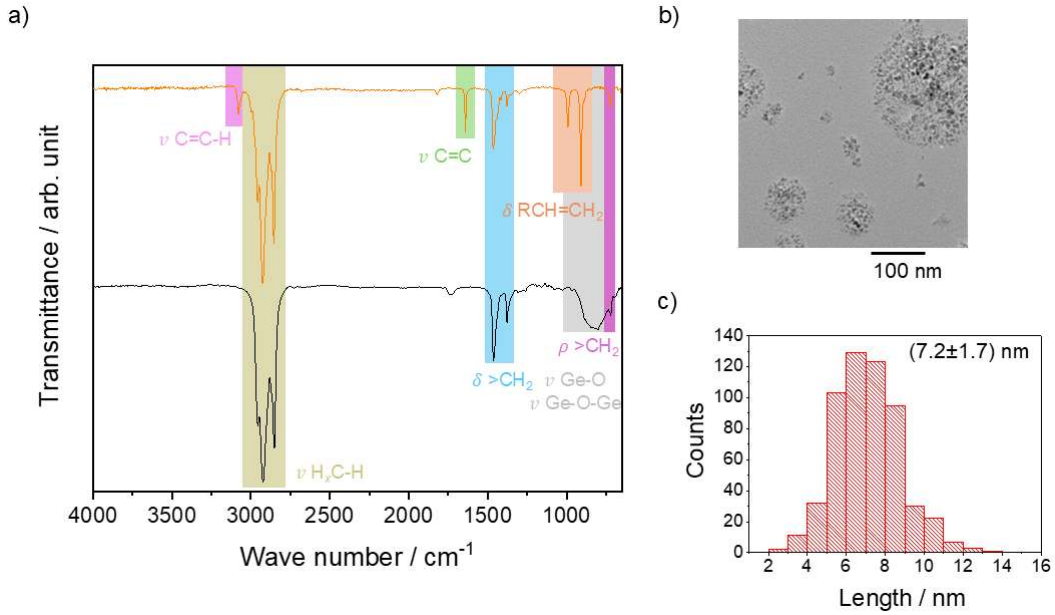

Figure 2. a) FTIR spectra of dodecyl-functionalized GeNCs (black line) and 1-dodecane (orange line) as a reference are depicted. Absorption bands being indicative of specific vibrational modes are highlighted. b) A representative TEM image of the dodecyl-functionalized GeNCs and the corresponding c) size distribution diagram illustrating the average particle size determined by counting at least 500 particles are shown.

3.2. Characterization of GeNC-Doped Specimen

Raman spectra of PP, GeNCs and GeNC/PP composites are summarized in **Figure 3**. Polypropylene exhibits a well-characterized Raman spectrum with distinct bands in both the fingerprint region (below $1500\ cm^{-1}$) and the high-frequency C–H stretching region ($2800 - 3000 cm^{-1}$) [55, 56].

 doi:10.20944/preprints202605.0524.v1

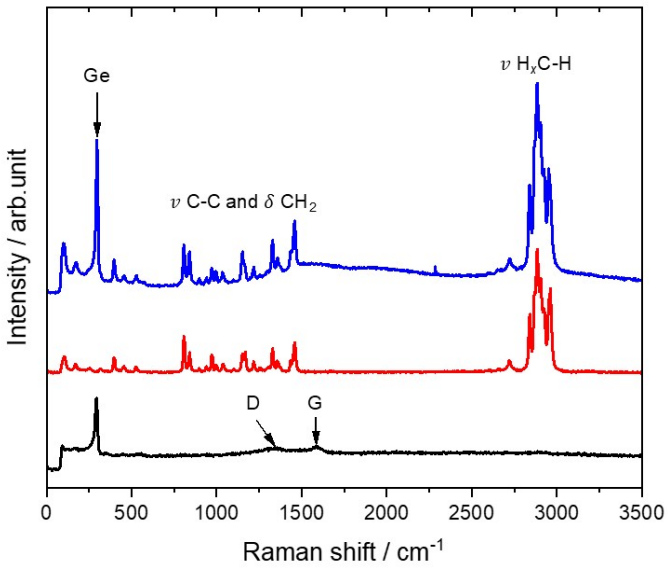

Figure 3. Raman spectra of dodecyl-functionalized GeNCs (black), polypropylene (red), and GeNC/PP composite material (blue). The composite spectrum exhibits characteristic vibrational signatures of both components.

In case of the functionalized GeNCs (**Figure 3**, black graph), a strong peak appears at $\sim 296\ cm^{-1}$ which corresponds to the Ge–Ge optical phonon mode, confirming the presence of crystalline germanium nanoparticles. In addition, two broad carbon-related bands are observed at approximately $\sim 1330\ cm^{-1}$ and $\sim 1590\ cm^{-1}$, corresponding to the D and G bands of graphitic carbon.

The Raman spectrum of the GeNC/PP composite (**Figure 3**, blue graph) combines the characteristic signatures of both constituents. The typical polypropylene bands remain visible in the fingerprint region between $\sim 800 - 1500\ cm^{-1}$, associated with C–C stretching vibrations and CH_2/CH_3 deformation modes, and between $\sim 2700 - 3000\ cm^{-1}$ due to distinct C–H stretching bands, while the Ge-related Raman band at $296\ cm^{-1}$ is additionally present (**Figure 3**). In contrast, pure PP (**Figure 3**, red graph) exhibits no Raman feature in this spectral region.

To investigate the nanoparticle distribution, Raman intensity maps of the $\sim 296\ cm^{-1}$ Ge–Ge band were recorded over an area of $30\ x\ 30\ \mu m^2$ ($80\ x\ 80$ pixels) for all samples (**Figure 4**). These false-color maps vividly illustrate how the Ge nanoparticles are distributed within the PP matrix. The pure PP sample B01 showed no detectable signal at $296\ cm^{-1}$ and only a homogeneous background with minor noise fluctuations (**Figure 4a**). In sample C01, containing the lowest GeNC concentration, isolated low-intensity spots appeared above the background (**Figure 4b**). These signals were spatially separated and sparsely distributed. For sample C02, the number and intensity of the Ge-related spots increased markedly (**Figure 4c**). The GeNC signals were more evenly distributed across the mapped area, although localized regions with several neighboring particles became visible. Finally, the highest loading sample (C03) exhibited a dense array of intense signals in the $296\ cm^{-1}$ map (**Figure 4d**). Several neighboring signals merged into larger regions of elevated intensity, indicating the formation of extended Ge-rich domains.

 doi:10.20944/preprints202605.0524.v1

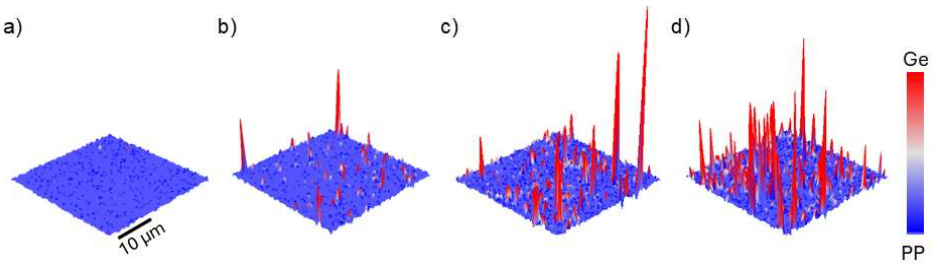

Figure 4. Raman intensity maps of the $\sim 296\ cm^{-1}$ Ge–Ge phonon mode for (a) pure PP (B01) and polypropylene composites with increasing GeNC loading: (b) C01, (c) C02, and (d) C03. The intensity scale (blue to red) corresponds to the charge coupled device (CCD) signal amplitude at the characteristic Ge Raman band. High-intensity regions in the generated images (displayed in red) correspond to locations with enhanced Ge Raman signal, indicating localized nanoparticle presence or increased scattering efficiency. All maps cover a $30\ x\ 30\ \mu m^2$ area.

Elemental Germanium has a well-known first-order Raman-active mode in the vicinity of $300\ cm^{-1}$. In the diamond-cubic crystal structure of Ge (often referred to as the Ge-I phase), the fundamental optical phonon gives rise to a Raman signal at approximately $300\ cm^{-1}$, corresponding to the Ge–Ge bond vibrational mode. For example, bulk crystalline Ge typically shows a sharp Raman band at $300\ cm^{-1}$, which is the longitudinal optical phonon mode of the Ge lattice [57]. When germanium is present as nanocrystals, the Raman features remain centered around the same general region but can exhibit slight shifts and broadening due to phonon confinement and strain effects. Notably, the principal Raman line for Ge nanoparticles is often reported near $\sim 297\ cm^{-1}$, a few cm^{-1} lower than the bulk value. This shift to $\sim 296\ cm^{-1}$ (and generally a broader peak) is a signature of nanocrystalline Ge. Indeed, one study of laser-synthesized GeNCs observed the Ge–Ge mode at about $293 - 297\ cm^{-1}$ for the nanocrystals, appearing as an asymmetric broadened peak [58, 59].

The prominent D ($\sim 1330\ cm^{-1}$) and G ($\sim 1590\ cm^{-1}$) C-bands appearing in the GeNC spectrum (**Figure 3**, black graph) indicate the presence of graphitic carbon species generated from the organic ligands. The emergence of these bands has been observed upon ligand breakdown, correlating with carbonaceous residue formation on the nanocrystals [60]. Such D/G features have been reported in similar systems after the decomposition of dodecyl ligands [61, 62].

The GeNC/PP composite spectra demonstrate that the Ge-related Raman signal can be clearly distinguished from the polypropylene matrix (**Figure 4**). Since pure PP does not exhibit any Raman band near $\sim 296\ cm^{-1}$, this resonance signal provides a highly selective spectral marker for the identification of GeNCs in the composite. The Ge–Ge band is therefore well suited as a tracer for the detection and localization of marker particles in polypropylene-based materials.

The Raman maps further reveal a concentration-dependent change in nanoparticle distribution. At low loading (C01), only isolated GeNC clusters are present, indicating that the nanoparticles remain largely separated within the matrix. Increasing GeNC concentration leads first to a more homogeneous distribution (C02), followed by the formation of larger agglomerated regions at the highest loading (C03). The increasing agglomeration at higher filling levels suggests a limit to physical dispersion.

Overall, the combined spectral and spatial analyses demonstrate that Ge nanocrystals can be reliably detected within polypropylene by Raman spectroscopy. Furthermore, the method is sufficiently sensitive to distinguish between different nanoparticle concentrations and dispersion states, making it suitable for the characterization of marker-based polymer compounds. The observed trends were consistent across multiple measurements (not shown), indicating a reproducible detection of Ge nanocrystals within the polymer matrix.

4. Conclusions

In this study, GeNC/PP composites were successfully synthesized starting from dodecyl-functionalized GeNCs via a solvent-based intercalation (blending) approach. Using an injection

 doi:10.20944/preprints202605.0524.v1

molding process based on a masterbatch composite, specimens with adjustable GeNC contents were prepared. The incorporation of GeNCs within the polypropylene matrix was confirmed by Raman spectroscopy, and the corresponding spectra clearly correlate with the varying germanium contents.

Raman spectroscopy provides a non-destructive and element-specific analytical method, in contrast to alternative techniques such as X-ray fluorescence (XRF) or laser-induced breakdown spectroscopy (LIBS). Furthermore, there are no spectral overlaps as there might be in other spectra such as M/NIR. The use of a confocal Raman microscope enables measurements with high spatial resolution, allowing detailed analysis of local GeNC distributions within the polymer matrix.

This study represents a proof of concept and demonstrates that under laboratory conditions the tunable, non-toxic, surface-functionalized Ge nanocrystals can be successfully integrated into polypropylene and reliably detected due to their distinct spectroscopic signatures.

Potential limitations of the presented approach in practical situations include influences on the Raman signal arising from the polymer matrix, such as fluorescence effects, as well as the presence of common additives, pigments, stabilizers, or recycled material fractions. In addition, the observed agglomeration behavior at higher concentrations, the determination of a minimum tracer concentration required for robust detection, and effects of varying the polymer matrix as well as NCs size represent important aspects that will be subjects of future research.

Further investigations into adapting the surface modification of the NCs and process optimizations in the compounding of the GeNC/PP composite, particularly with regard to very low, tracer-relevant concentrations, are necessary and should include the effect of multiple recycling cycles on tracer detectability. Future work should also focus on identifying the limits of measurement times under application-relevant conditions.

Supplementary Materials: The following supporting information can be downloaded at the website of this paper posted on Preprints.org. Figure S1: X-ray diffraction analysis of dodecyl functionalized GeNCs ; Figure S2: X-ray photoelectron spectroscopy of dodecyl functionalized GeNCs; Figure S3: Raman spectroscopy of dodecyl functionalized GeNCs; Figure S4: Raman spectroscopy mapping of GeNC/PP composites.

Author Contributions: Conceptualization, P. K., M. H. and J. V.; methodology, C. K. M. and M. H.; validation, C. K. M.; formal analysis, M. P. and C. K. M.; investigation, M. G., M. P., P. K., A. L. and C.K. M.; data curation, M. P. and C. K. M.; writing—original draft preparation, M. G., M. P., P. K. and C. K. M.; writing—review and editing, M. G., M. P., P. K., A. L., C. K. M., J. V. and M. H.; visualization, M. G., M. P., P. K. and C. K. M.; supervision, M. H.; project administration, M. H.. All authors have read and agreed to the published version of the manuscript.

Funding: This research was partly funded by the European Social Fund (ESF) and the Free State of Saxony within the framework of the Landesinnovationspromotion program, application number 100670550 and P. Kitschke gratefully acknowledges financial support by the Deutsche Akademie der Naturforscher Leopoldina – Nationale Akademie der Wissenschaften for a Leopoldina Postdoc-Fellowship. The APC was funded by Projekt DEAL.

Data Availability Statement: The original contributions presented in this study are included in the article or the Supplementary Material. Additional information can be requested from the authors.

Acknowledgments: The authors thank Thermo Fisher Scientific in Karlsruhe and especially Mr. Reynel Humberto Gomez Alfonso for experimental support.

Conflicts of Interest: The authors declare no conflicts of interest. The funders had no role in the design of the study; in the collection, analyses, or interpretation of data; in the writing of the manuscript; or in the decision to publish the results.

Abbreviations

The following abbreviations are used in this manuscript:

CCD	charge coupled device
EDX	energy dispersive X-ray

 doi:10.20944/preprints202605.0524.v1

FTIR	fourier transform infrared
FWHM	full width of the diffraction line at half of the maximum intensity
LIBS	laser-induced breakdown
MIR	mid infrared
NCs	nanocrystals
NIR	near-infrared
PP	polypropylene
PPWR	packaging and Packaging Waste Regulation
PTFE	polytetrafluorethylen
PVA	polyvinyl alcohol
PXRD	X-ray powder diffraction
TBS	tracer-based sorting
TEM	transmission electron microscopy
XPS	X-ray photoelectron spectroscopy
XRFS	X-ray fluorescence

References

1. Environment Packaging waste. https://environment.ec.europa.eu/topics/waste-and-recycling/packaging-waste_en (24 November 2025).
2. EUR-Lex - 52020DC0098 - EN - EUR-Lex. https://eur-lex.europa.eu/legal-content/EN/TXT/?uri=COM%3A2020%3A98%3AFIN (24 November 2025).
3. Dokl, M., Copot, A., Krajnc, D., van Fan, Y., Vujanović, A., Aviso, K.B., Tan, R.R., Kravanja, Z., Čuček, L. (2024) Global projections of plastic use, end-of-life fate and potential changes in consumption, reduction, recycling and replacement with bioplastics to 2050. *Sustainable Production and Consumption*, **51**, 498–518, DOI: 10.1016/j.spc.2024.09.025.
4. PlasticsEurope (2024) The Circular Economy for Plastics: A European Analysis.
5. Rozenstein, O., Puckrin, E., Adamowski, J. (2017) Development of a new approach based on midwave infrared spectroscopy for post-consumer black plastic waste sorting in the recycling industry. *Waste management (New York, N.Y.)*, **68**, 38–44, DOI: 10.1016/j.wasman.2017.07.023.
6. Abts, G. (2020) *Kunststoff-Wissen für Einsteiger: Grundlagen, Eigenschaften und Recycling polymerer Werkstoffe*, 4th edn, Carl Hanser Verlag GmbH & Co. KG, München, DOI: 10.3139/9783446474888.
7. Araujo-Andrade, C., Bugnicourt, E., Philippet, L., Rodriguez-Turienzo, L., Nettleton, D., Hoffmann, L., Schlummer, M. (2021) Review on the photonic techniques suitable for automatic monitoring of the composition of multi-materials wastes in view of their posterior recycling. *Waste management & research : the journal of the International Solid Wastes and Public Cleansing Association, ISWA*, **39** (5), 631–651, DOI: 10.1177/0734242X21997908.
8. Luttermann, K.D.P., Claussen, U., Sayed, A.E., Riess, R. (1991) Method for the masking of plastics. EP0476416 (A2), filed Sep. 3, 1991 and issued Mar. 25, 1992.
9. Hallaji, Z., Bagheri, Z., Ranjbar, B. (2023) The role of fluorescent carbon dots in the fate of plastic waste. *Journal of Environmental Chemical Engineering*, **11** (5), 110322, DOI: 10.1016/j.jece.2023.110322.
10. Bezati, F., Froelich, D., Massardier, V., Maris, E. (2011) Addition of X-ray fluorescent tracers into polymers, new technology for automatic sorting of plastics: Proposal for selecting some relevant tracers. *Resources, Conservation and Recycling*, **55** (12), 1214–1221, DOI: 10.1016/j.resconrec.2011.05.014.
11. Müssig, S., Fidler, F., Haddad, D., Hiller, K.-H., Wintzheimer, S., Mandel, K. (2019) Supraparticles with a Magnetic Fingerprint Readable by Magnetic Particle Spectroscopy: An Alternative beyond Optical Tracers. *Adv Materials Technologies*, **4** (9), DOI: 10.1002/admt.201900300.
12. Kuřitka, I., Sedlařík, V., Harea, D., Harea, E., Urbánek, P., Šloufová, I., Coufal, R., Zedník, J. (2020) Polymer Labelling with a Conjugated Polymer-Based Luminescence Probe for Recycling in the Circular Economy. *Polymers*, **12** (6), DOI: 10.3390/polym12061226.
13. Reiss, P., Carrière, M., Lincheneau, C., Vaure, L., Tamang, S. (2016) Synthesis of Semiconductor Nanocrystals, Focusing on Nontoxic and Earth-Abundant Materials. *Chemical reviews*, **116** (18), 10731–10819, DOI: 10.1021/acs.chemrev.6b00116.

 doi:10.20944/preprints202605.0524.v1

14. Carolan, D. (2017) Recent advances in germanium nanocrystals: Synthesis, optical properties and applications. *Progress in Materials Science*, **90**, 128–158, DOI: 10.1016/j.pmatsci.2017.07.005.
15. Schmid, G. (ed) (2010) *Nanoparticles: From theory to application*, 2nd edn, Wiley-VCH, Weinheim, DOI: 10.1002/9783527631544.
16. Wang, D., Yin, F., Du, Z., Han, D., Tang, J. (2019) Recent progress in quantum dot-sensitized solar cells employing metal chalcogenides. *J. Mater. Chem. A*, **7** (46), 26205–26226, DOI: 10.1039/C9TA10557C.
17. Leger, H.S. (2022) OLED vs QLED: Which TV tech is the best? *TechRadar*.
18. Roco, M.C. (2018) Overview, in *Nanotechnology commercialization: Manufacturing processes and products* (eds T.O. Mensah, B. Wang, G. Bothun, J. Winter, V. Davis), Wiley, Hoboken, NJ, pp. 1–23, DOI: 10.1002/9781119371762.ch1.
19. Hu, X.-L., Kwon, N., Yan, K.-C., Sedgwick, A.C., Chen, G.-R., He, X.-P., James, T.D., Yoon, J. (2020) Bio-Conjugated Advanced Materials for Targeted Disease Theranostics. *Adv Funct Materials*, **30** (13), DOI: 10.1002/adfm.201907906.
20. Zhao, Y., Zhou, H., Zhang, S., Xu, J. (2019) The synthesis of metal nanoclusters and their applications in bio-sensing and imaging. *Methods and applications in fluorescence*, **8** (1), 12001, DOI: 10.1088/2050-6120/ab57e7.
21. McVey, B.F.P., Prabakar, S., Gooding, J.J., Tilley, R.D. (2017) Solution Synthesis, Surface Passivation, Optical Properties, Biomedical Applications, and Cytotoxicity of Silicon and Germanium Nanocrystals. *ChemPlusChem*, **82** (1), 60–73, DOI: 10.1002/cplu.201600207.
22. You, S., Zeng, H., Ku, Z., Wang, X., Wang, Z., Rong, Y., Zhao, Y., Zheng, X., Luo, L., Li, L., Zhang, S., Li, M., Gao, X., Li, X. (2020) Multifunctional Polymer-Regulated SnO2 Nanocrystals Enhance Interface Contact for Efficient and Stable Planar Perovskite Solar Cells. *Advanced materials (Deerfield Beach, Fla.)*, **32** (43), e2003990, DOI: 10.1002/adma.202003990.
23. Parravicini, J., Di Trapani, F., Nelson, M.D., Rex, Z.T., Beiter, R.D., Catelani, T., Acciarri, M.F., Podesta, A., Lenardi, C., Binetti, S.O., Di Vece, M. (2020) Quantum Confinement in the Spectral Response of n-Doped Germanium Quantum Dots Embedded in an Amorphous Si Layer for Quantum Dot-Based Solar Cells. *ACS Appl. Nano Mater.*, **3** (3), 2813–2821, DOI: 10.1021/acsanm.0c00125.
24. Matter, F., Niederberger, M., Putz, F. (2021) Colloidal Nanocrystals: A Toolbox for Materials Chemistry. *Chimia*, **75** (5), 387–397, DOI: 10.2533/chimia.2021.387.
25. Vaughn, D.D. and Schaak, R.E. (2013) Synthesis, properties and applications of colloidal germanium and germanium-based nanomaterials. *Chemical Society reviews*, **42** (7), 2861–2879, DOI: 10.1039/c2cs35364d.
26. Fan, J. and Chu, P.K. (2010) Group IV nanoparticles: synthesis, properties, and biological applications. *Small (Weinheim an der Bergstrasse, Germany)*, **6** (19), 2080–2098, DOI: 10.1002/smll.201000543.
27. Yu, H., Thiessen, A.N., Hossain, M.A., Kloberg, M.J., Rieger, B., Veinot, J.G.C. (2020) Thermally Induced Dehydrogenative Coupling of Organosilanes and H-Terminated Silicon Quantum Dots onto Germanane Surfaces. *Chem. Mater.*, **32** (11), 4536–4543, DOI: 10.1021/acs.chemmater.0c00482.
28. Robidillo, C.J.T. and Veinot, J.G.C. (2020) Functional Bio-inorganic Hybrids from Silicon Quantum Dots and Biological Molecules. *ACS applied materials & interfaces*, **12** (47), 52251–52270, DOI: 10.1021/acsami.0c14199.
29. Islam, M.A., Sinelnikov, R., Howlader, M.A., Faramus, A., Veinot, J.G.C. (2018) Mixed Surface Chemistry: An Approach to Highly Luminescent Biocompatible Amphiphilic Silicon Nanocrystals. *Chem. Mater.*, **30** (24), 8925–8931, DOI: 10.1021/acs.chemmater.8b04227.
30. Mobarok, M.H., Purkait, T.K., Islam, M.A., Miskolzie, M., Veinot, J.G.C. (2017) Instantaneous Functionalization of Chemically Etched Silicon Nanocrystal Surfaces. *Angewandte Chemie (International ed. in English)*, **56** (22), 6073–6077, DOI: 10.1002/anie.201609651.
31. Islam, M.A., Mobarok, M.H., Sinelnikov, R., Purkait, T.K., Veinot, J.G.C. (2017) Phosphorus Pentachloride Initiated Functionalization of Silicon Nanocrystals. *Langmuir : the ACS journal of surfaces and colloids*, **33** (35), 8766–8773, DOI: 10.1021/acs.langmuir.7b00518.
32. Sinelnikov, R., Dasog, M., Beamish, J., Meldrum, A., Veinot, J.G.C. (2017) Revisiting an Ongoing Debate: What Role Do Surface Groups Play in Silicon Nanocrystal Photoluminescence? *ACS Photonics*, **4** (8), 1920–1929, DOI: 10.1021/acsphotonics.7b00102.

 doi:10.20944/preprints202605.0524.v1

33. Höhlein, I.M.D., Angı, A., Sinelnikov, R., Veinot, J.G.C., Rieger, B. (2015) Functionalization of hydride-terminated photoluminescent silicon nanocrystals with organolithium reagents. *Chemistry (Weinheim an der Bergstrasse, Germany)*, **21** (7), 2755–2758, DOI: 10.1002/chem.201405555.
34. Höhlein, I.M.D., Kehrle, J., Helbich, T., Yang, Z., Veinot, J.G.C., Rieger, B. (2014) Diazonium salts as grafting agents and efficient radical-hydrosilylation initiators for freestanding photoluminescent silicon nanocrystals. *Chemistry (Weinheim an der Bergstrasse, Germany)*, **20** (15), 4212–4216, DOI: 10.1002/chem.201400114.
35. Höhlein, I.M.D., Kehrle, J., Purkait, T.K., Veinot, J.G.C., Rieger, B. (2015) Photoluminescent silicon nanocrystals with chlorosilane surfaces--synthesis and reactivity. *Nanoscale*, **7** (3), 914–918, DOI: 10.1039/c4nr05888g.
36. Dasog, M. and Veinot, J.G.C. (2014) Tuning silicon quantum dot luminescence via surface groups. *Physica Status Solidi (b)*, **251** (11), 2216–2220, DOI: 10.1002/pssb.201400026.
37. Dasog, M., los Reyes, G.B. de, Titova, L.V., Hegmann, F.A., Veinot, J.G.C. (2014) Size vs surface: tuning the photoluminescence of freestanding silicon nanocrystals across the visible spectrum via surface groups. *ACS nano*, **8** (9), 9636–9648, DOI: 10.1021/nn504109a.
38. Dasog, M., Yang, Z., Regli, S., Atkins, T.M., Faramus, A., Singh, M.P., Muthuswamy, E., Kauzlarich, S.M., Tilley, R.D., Veinot, J.G.C. (2013) Chemical insight into the origin of red and blue photoluminescence arising from freestanding silicon nanocrystals. *ACS nano*, **7** (3), 2676–2685, DOI: 10.1021/nn4000644.
39. Beri, D. (2023) Silicon quantum dots: surface matter, what next? *Mater. Adv.*, **4** (16), 3380–3398, DOI: 10.1039/D2MA00984F.
40. Javadi, M., Picard, D., Sinelnikov, R., Narreto, M.A., Hegmann, F.A., Veinot, J.G.C. (2017) Synthesis and Surface Functionalization of Hydride-Terminated Ge Nanocrystals Obtained from the Thermal Treatment of Ge(OH)2. *Langmuir : the ACS journal of surfaces and colloids*, **33** (35), 8757–8765, DOI: 10.1021/acs.langmuir.7b00358.
41. Ounkaew, A., Antoniuk, D., Veinot, J.G.C., Bouvier, M., Constantinescu, I., Tees-DeBeyer, W., Hung, S., Kizhakkedathu, J.N., Narain, R. (2025) Biocompatible Water-Soluble Silicon Quantum Dots for Photodynamic Cancer Therapy. *ACS Appl. Nano Mater.*, **8** (42), 20397–20410, DOI: 10.1021/acsanm.5c03568.
42. Kustov, P., Petrova, E., Nazarov, M., Gilmullin, A., Sandomirskii, M., Ponkratova, E., Yaroshenko, V., Ageev, E., Zuev, D. (2022) Mie-Resonant Silicon Nanoparticles for Physically Unclonable Anti-Counterfeiting Labels. *ACS Appl. Nano Mater.*, **5** (8), 10548–10559, DOI: 10.1021/acsanm.2c01878.
43. Marinins, A., Zandi Shafagh, R., van der Wijngaart, W., Haraldsson, T., Linnros, J., Veinot, J.G.C., Popov, S., Sychugov, I. (2017) Light-Converting Polymer/Si Nanocrystal Composites with Stable 60-70% Quantum Efficiency and Their Glass Laminates. *ACS applied materials & interfaces*, **9** (36), 30267–30272, DOI: 10.1021/acsami.7b09265.
44. Dasog, M., Kehrle, J., Rieger, B., Veinot, J.G.C. (2016) Silicon Nanocrystals and Silicon-Polymer Hybrids: Synthesis, Surface Engineering, and Applications. *Angewandte Chemie (International ed. in English)*, **55** (7), 2322–2339, DOI: 10.1002/anie.201506065.
45. Yang, Z., Dasog, M., Dobbie, A.R., Lockwood, R., Zhi, Y., Meldrum, A., Veinot, J.G.C. (2014) Highly Luminescent Covalently Linked Silicon Nanocrystal/Polystyrene Hybrid Functional Materials: Synthesis, Properties, and Processability. *Adv Funct Materials*, **24** (10), 1345–1353, DOI: 10.1002/adfm.201302091.
46. Kortshagen, U., Anthony, R., Gresback, R., Holman, Z., Ligman, R., Liu, C.-Y., Mangolini, L., Campbell, S.A. (2008) Plasma synthesis of group IV quantum dots for luminescence and photovoltaic applications. *Pure and Applied Chemistry*, **80** (9), 1901–1908, DOI: 10.1351/pac200880091901.
47. Cardoso, J., Marom, S., Mayer, J., Modi, R., Podestà, A., Xie, X., van Huis, M.A., Di Vece, M. (2018) Germanium Quantum Dot Grätzel-Type Solar Cell. *Physica Status Solidi (a)*, **215** (24), DOI: 10.1002/pssa.201800570.
48. Nigro, A., Jutzi, E., Oppliger, F., Palma, F. de, Olsen, C., Ruiz-Caridad, A., Gadea, G., Scarlino, P., Zardo, I., Hofmann, A. (2024) Demonstration of Microwave Resonators and Double Quantum Dots on Optimized Reverse-Graded Ge/SiGe Heterostructures. *ACS applied electronic materials*, **6** (7), 5094–5100, DOI: 10.1021/acsaelm.4c00654.

 doi:10.20944/preprints202605.0524.v1

49. Tidjani, H., Tosato, A., Ivlev, A., Déprez, C., Oosterhout, S., Stehouwer, L., Sammak, A., Scappucci, G., Veldhorst, M. (2023) Vertical gate-defined double quantum dot in a strained germanium double quantum well. *Phys. Rev. Applied*, **20** (5), DOI: 10.1103/PhysRevApplied.20.054035.
50. Ortaç, B., Kayaci, F., Vural, H.A., Deniz, A.E., Uyar, T. (2013) Photoluminescent electrospun polymeric nanofibers incorporating germanium nanocrystals. *Reactive and Functional Polymers*, **73** (9), 1262–1267, DOI: 10.1016/j.reactfunctpolym.2013.06.007.
51. Javadi, M., Michaelis, V.K., Veinot, J.G.C. (2018) Thermally Induced Evolution of "Ge(OH) 2 ": Controlling the Formation of Oxide-Embedded Ge Nanocrystals. *J. Phys. Chem. C*, **122** (30), 17518–17525, DOI: 10.1021/acs.jpcc.8b04640.
52. OriginLab OriginLab Releases Origin 2016 Data Analysis and Graphing Software. https://www.originlab.com/index.aspx?go=Company/NewsAndEvents/PressRoom&pid=3209 (26 November 2025).
53. Software Informer PerkinElmerInformatics ChemDraw Professional. https://perkinelmer-chemdraw-professional.software.informer.com/15.1/ (26 November 2025).
54. Henderson, E.J., Hessel, C.M., Veinot, J.G.C. (2008) Synthesis and photoluminescent properties of size-controlled germanium nanocrystals from phenyl trichlorogermane-derived polymers. *Journal of the American Chemical Society*, **130** (11), 3624–3632, DOI: 10.1021/ja710286a.
55. Arruebarrena de Báez, M., Hendra, P., Judkins, M. (1995) The Raman spectra of oriented isotactic polypropylene. *Spectrochimica Acta Part A: Molecular and Biomolecular Spectroscopy*, **51** (12), 2117–2124, DOI: 10.1016/0584-8539(95)01512-1.
56. Perraki, M., Skliros, V., Mecaj, P., Vasileiou, E., Salmas, C., Papanikolaou, I., Stamatis, G. (2024) Identification of Microplastics Using μ-Raman Spectroscopy in Surface and Groundwater Bodies of SE Attica, Greece. *Water*, **16** (6), 843, DOI: 10.3390/w16060843.
57. Volodin, V.A., Marin, D.V., Sachkov, V.A., Gorokhov, E.B., Rinnert, H., Vergnat, M. (2014) Applying an improved phonon confinement model to the analysis of Raman spectra of germanium nanocrystals. *J. Exp. Theor. Phys.*, **118** (1), 65–71, DOI: 10.1134/S1063776114010208.
58. Gao, X., Luo, W., Zhong, C., Wexler, D., Chou, S.-L., Liu, H.-K., Shi, Z., Chen, G., Ozawa, K., Wang, J.-Z. (2014) Novel germanium/polypyrrole composite for high power lithium-ion batteries. *Sci Rep*, **4**, 6095, DOI: 10.1038/srep06095.
59. Liu, J., Liang, C., Tian, Z., Zhang, S., Shao, G. (2013) Spontaneous Growth and Chemical Reduction Ability of Ge Nanoparticles. *Sci Rep*, **3** (1), DOI: 10.1038/srep01741.
60. Sperry, B.M., Kukhta, N.A., Huang, Y., Luscombe, C.K. (2023) Ligand Decomposition during Nanoparticle Synthesis: Influence of Ligand Structure and Precursor Selection. *Chem. Mater.*, **35** (2), 570–583, DOI: 10.1021/acs.chemmater.2c03006.
61. Watts, J.A., Fay, M.W., Rance, G.A., Brown, P.D., Khlobystov, A.N. (2018) Formation of hollow carbon nanoshells from thiol stabilised silver nanoparticles via heat treatment. *Carbon*, **139**, 538–544, DOI: 10.1016/j.carbon.2018.06.074.
62. Lu, Q., Zhong, Y., Zhou, W., Liao, K., Shao, Z. (2018) Dodecylamine-Induced Synthesis of a Nitrogen-Doped Carbon Comb for Advanced Lithium–Sulfur Battery Cathodes. *Adv Materials Inter*, **5** (9), DOI: 10.1002/admi.201701659.